INTERNATIONAL SOCIETY FOR SOIL MECHANICS AND GEOTECHNICAL ENGINEERING



This paper was downloaded from the Online Library of the International Society for Soil Mechanics and Geotechnical Engineering (ISSMGE). The library is available here:

https://www.issmge.org/publications/online-library

This is an open-access database that archives thousands of papers published under the Auspices of the ISSMGE and maintained by the Innovation and Development Committee of ISSMGE.

The paper was published in the proceedings of the 20th International Conference on Soil Mechanics and Geotechnical Engineering and was edited by Mizanur Rahman and Mark Jaksa. The conference was held from May 1st to May 5th 2022 in Sydney, Australia.

Development and application of a GPGPU-parallelized hybrid finite-discrete element method for modelling geo-structure collapse and resultant debris flow

Hongyuan Liu

School of Engineering, University of Tasmania, Australia, hong.liu@utas.edu.au

Daisuke Fukuda

Faculty of Engineering, Hokkaido University, Japan

ABSTRACT: FDEM is seldom implemented to model non-cohesive soils due to intensive computational costs required for contact detections and interactions of irregular-shaped non-cohesive soil particles. This study first reviews a series of aut hors' recent developments for speeding up the contact detections and interactions for FDEM including GPGPU-parallelization, efficient contact activation approach, mass scaling, hyperplane separation theorem, as well as adaptive and semi-adaptive contact activation scheme. With them implemented, our GPGPU-parallelized HFDEM is about 8,000 to 61,000 times faster than sequential FDEM code, which paves the way for investigating the instability and collapse of geo-structures and resultant debris fragmentation and flow involving in a large number of irregular-shaped non-cohesive debris. The GP GPU-parallelized HFDEM is then implemented to investigate the collapse process of 3D irregular-shaped and non-cohesive soils heaps under gravity, and the excavation-induced slope instability as well as the resultant complex debris fragment ation and flow process.

RÉSUMÉ: Le FDEM est rarement mis en œuvre pour modéliser des sols non cohésifs en raison des coûts de calcul intensifs requis pour les détections de contact et les interactions de particules de sol non cohésives de forme irrégulière. Cette étude passe d'abord en revue une série de développements d'auteurs pour accélérer les détections de contact et les interactions pour FDEM, y compris la parallélisation GPGPU, l'approche d'activation de contact efficace, la mise à l'échelle de masse, le théorème de séparation d'hyperplan, ainsi que le schéma d'activation de contact adaptatif et semi-adaptatif. Avec leur mise en œuvre, notre HFDEM parallélisé GPGPU est environ 8000 à 61000 fois plus rapide que le code FDEM séquentiel, ce qui ouvre la voie à l'étude de l'instabilité et de l'effondrement des géo-structures et de la fragmentation et des flux de débris résultants impliquant un grand nombre de débris non cohésifs en forme. Le HFDEM parallélisé par GPGPU est ensuite mis en œuvre pour étudier le processus d'effondrement des tas de sols de forme irrégulière et non cohésive 3D sous gravité, et l'instabilité de la pente induite par l'excavation ainsi que le processus complexe de fragmentation et d'écoulement des débris qui en résulte.

KEYWORDS: FDEM, geo-structure collapse, slope instability, debris flow, and irregular-shaped non-cohesive particles.

1 INTRODUCTION

More and more geotechnical infrastructures such as underground metro systems, hydropower plants and highways have been being built during recent decades. Correspondingly, engineering disasters, such as tunnel collapse and slope failure, have occurred from time to time. The study of geomaterial damage and failure mechanism is the key to understanding geo-structure stability and preventing possible geo-disasters.

With rapid developments of computer power, interactive computer graphics and topological data structures, numerical methods have been a robust tool to investigate geomaterial damage and failure. Among them, the combined finite-discrete element method (FDEM), initially proposed by Munjiza et al. (1995), incorporates the advantages of the most advanced continuous and discontinuous methods and thus can naturally model the transition from continuum to discontinuum during material damage and failure. Correspondingly, FDEM has been applied and further developed by a number of researchers around the world to simulate the damage and fragmentation of civil engineering materials and the collapse and fragmentation of civil engineering structures, especially since the first two-dimensional (2D) open-source FDEM software, i.e. the Y2D code, was made available to the research community (Munjiza, 2004).

However, most of these studies apply FDEM in rock mechanics (Latham et al., 2013; Rougier et al., 2014; Lisjak et al., 2018; Fukuda et al., 2020) and few researchers have applied FDEM into soil mechanics. Moreover, due to the nature of intensive computations involved in contact detections and

interactions of complex discrete rock fragments, FDEM has only been applied to model small-scale rock failures in laboratory and has seldom been capable of investigating the instability and collapse of large-scale geotechnical engineering structures. Correspondingly, this paper intends to apply a self-developed hybrid FDEM parallelized on the basis of the general-purpose graphic-process-unit (GPGPU) using the compute unified device architecture (CUDA) C/C++ in investigating geostructures collapse and resultant debris fragmentation and flow.

2 GPGPU-PARALLELIZED HYBRID FINITE-DISCRETE ELEMENT METHOD

An integrated development environment (IDE) of both twodimensional (2D) and three-dimensional (3D) hybrid finitediscrete element method (HFDEM) has been developed by the authors (Liu et al., 2015) and has been applied to model a series of applications involving in geomaterial damage, failure and collapse (Liu et al., 2016; An et al., 2017). To overcome the computationally expensive issue of FDEM, the authors (Fukuda et al., 2019 & 2020) recently parallelized the HFDEM IDE2D/3D code on the basis of GPGPU using CUDA C/C++. The detailed computing performance analysis shows the GPGPU-parallelized HFDEM 2D/3D IDE code can achieve the maximum speedups of 128.6 and 286 times in the case of the 2D and 3D modellings, respectively. More recently, adaptive efficient contact activation (Mohammadnejad et al., 2020), mass scaling, hyperplane separation theorem and semi-adaptive contact activation approach (Fukuda et al., 2021) have been implemented by the authors to further speed up GPGPU-parallelized HFDEM. Rough

estimation has shown our GPGPU-parallelized HFDEM is about 8,165 to 61,344 times faster than the sequential FDEM code, which paves the way for investigating the instability and collapse of large-scale geotechnical engineering structures using the 2D and even 3D FDEM.

This section introduces the further developments of the efficient contact interactions between any arbitrary-shaped particles, the insertion of cohesive joints inside each particle and cohesive-less joints between the particles, and the local damping while the fundamental theory and detailed implementation of the GPGPU-parallelized HFDEM2D/3D software can be found in the authors' former publications (Fukuda et al., 2019 & 2020). In the FDEM, the numerical model is considered to consist of a single discrete particle or a number of interactive discrete particles such as those shown in Fig. 1. Each discrete particle is of a general shape and size and is modelled by a single discrete element. Each discrete element is then discretized into finite elements to analyze deformability, failure and fracture, thus imposing no additional requirements on handling the geometry and interaction of individual discrete particles, which have advantages over purely discrete element method such as PFC and UDEC.

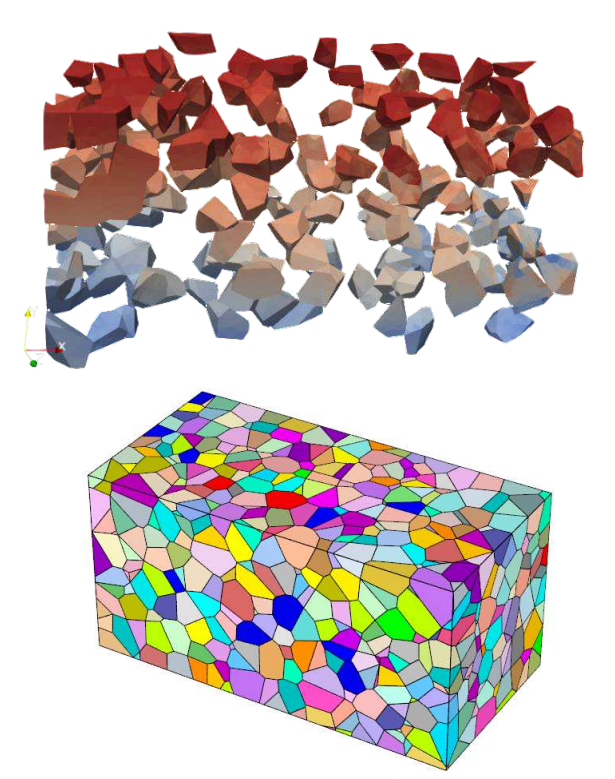


Figure 1. Particles in the finite-discrete element model: a) discrete particles and b) densely packed particles.

The contact between the discrete particles is essentially that between the tetrahedral elements in 3D or the triangular elements in 2D, which is modelled using the penalty method. For example, when any two tetrahedral elements subjected to contact detection are found to overlap each other, the contact potential due to the overlapping of two elements is exactly computed. The normal contact force, f_{con_n} , is then computed for each contacting couple, which acts normally to the contact surface and is proportional to the contact potential. The proportional factor is called the normal "contact penalty", P_{n_con} . After the normal contact force, f_{con_n} , and its acting point are obtained, the nominal normal overlap, o_n , and relative displacement vector, Δu_{slide} , at the acting point of $f_{con n}$ are readily computed. After $f_{con n}$ is determined, the magnitude of the tangential contact force vector, $||\mathbf{f}_{con tan}||$, is computed according to the classical Coulomb friction law. The $||\mathbf{f}_{con_tan}||$ is computed based on Eq. 1:

$$\|\mathbf{f}_{\text{con tan}}\| = \mu_{\text{fric}} f_{\text{con n}} \tag{1}$$

where $\mu_{\rm fric}$ is the friction coefficient between the contact surfaces. The tangential contact force, $f_{\rm con_tan}$, is applied parallel to the contact surface in the opposite direction to $\Delta u_{\rm slide}$. In the full contact activation approach, all elements in the model domain are subjected to contact interaction force calculations above, which is inefficient and rather time consuming, especially in the case that no failures of the particles occur. An adaptive contact activation approach is then proposed, in which, only the tetrahedral elements in the model boundary and in the vicinity of newly failed cohesive elements become contact candidates and are added to the contact detection list, as shown in Fig. 2.

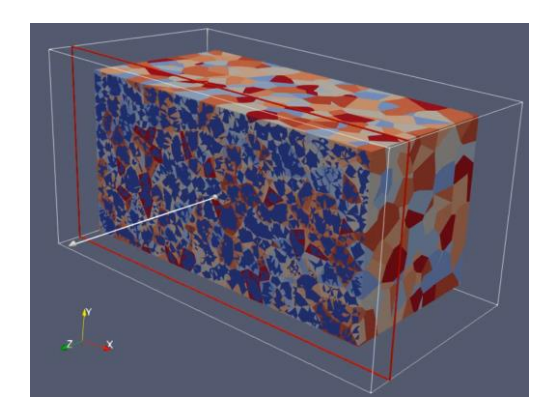


Figure 2. Adaptive contact activation approach: deep blue represents the elements without subjecting to contact calculation while other colors represents the elements subjected to contact calculation.

One advantage of the adaptive contact activation approach is that the contact detection and contact force calculations are necessary only for the initial material surfaces until the failures occur, which makes the dramatic savings of the computational time compared with the full contact activation approach. However, the adaptive contact activation approach suffers from numerical instabilities characterized by spurious fracture mode. It has been proven by the authors (Fukuda et al., 2021) that the spurious fracture mode is due to the topological inconsistency of the mesh caused by shear softening of cohesive elements. Correspondingly, a semi-adaptive contact activation approach is developed by the authors (Fukuda et al., 2021) to overcome the numerical instability when the state of the cohesive elements just enters the shear softening regime and the damage variable just satisfies a certain threshold. In this way, the semi-adaptive contact activation approach overcomes not only the spurious fracture mode but also the time-consuming contact interaction calculation.

Initially discrete particles such as soils, rock aggregates and rock fragments can be modelled by inserting cohesive-less elements between the discrete particles while the failure and fracture of the discrete particles are modelled using cohesive elements, which is another advantage of FDEM over other numerical methods. Fig. 3 depicts the constitutive behaviors of cohesive elements implemented in FDEM, in which the normal and shear cohesive tractions, ($\sigma^{\rm coh}$ and $\tau^{\rm coh}$, respectively), acting on each face of the cohesive elements are computed using Eqs. 2-3 and 4-5 assuming tensile and shear softening behaviors, respectively:

$$\sigma^{coh} = \begin{cases} \frac{2o}{o_{overlap}} T_S & o < 0\\ g(o)f(D)T_S & 0 \le o \le o_p\\ f(D)T_S & o > o_n \end{cases}$$
 (2)

$$g(o) = \left[\frac{2o}{o_p} - \left(\frac{o}{o_p}\right)^2\right] \tag{3}$$

$$\tau^{coh} = \begin{cases} g(s)[f(D)c - \sigma^{coh}tan\emptyset] & 0 \le |s| \le s_p \\ f(D)c - \sigma^{coh}tan\emptyset & s_p < |s| \end{cases} \tag{4}$$

$$g(s) = \left[\frac{2|s|}{s_p} - \left(\frac{|s|}{s_p}\right)^2\right] \tag{5}$$

where o_p and s_p are the elastic limits of the opening displacement o and the shear displacement s, respectively, o_{overlap} is the representative overlap when o is negative, T_s is the tensile strength of the cohesive element, c is the cohesion, and ϕ is the internal friction angle. Positive o and σ^{coh} values indicate crack opening and a tensile cohesive traction, respectively. Eq. 4 corresponds to the Mohr-Coulomb shear strength model with a tension cut-off. The cohesive tractions σ^{coh} and τ^{coh} are applied to the opposite directions of the relative opening and sliding in the cohesive elements, respectively.

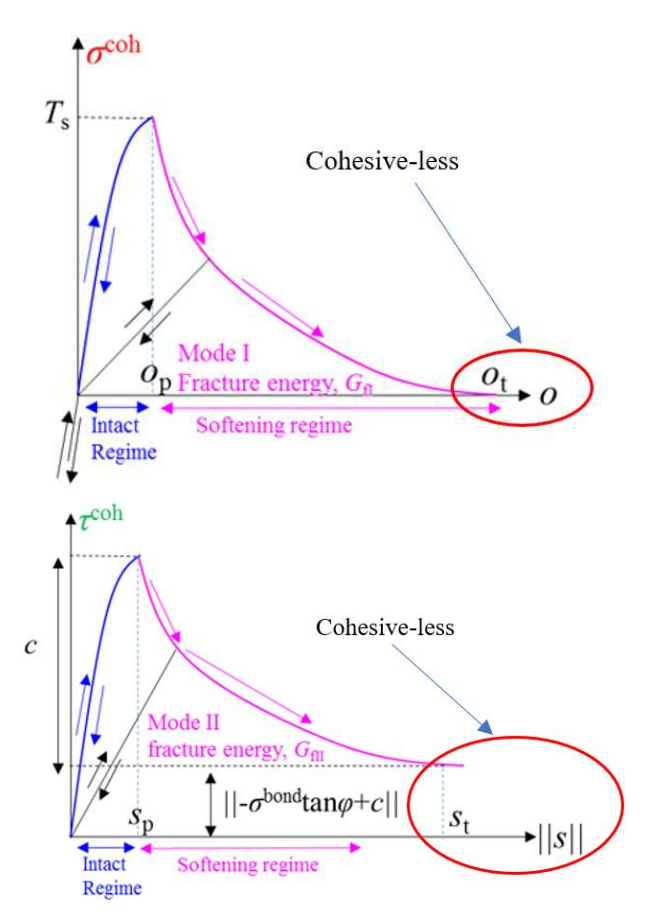


Figure 3. Constitutive behaviors of cohesive elements

As can be seen from Fig. 3, the cohesive elements become cohesive-less when $o \ge o_t$ and $\|s\| \ge s_t$ in the case of tensile and shear behaviours, respectively. Similar to the cohesive-less elements, the interaction between the cohesive-less phases of the cohesive elements is modelled by the penalty method, in which the contact potential due to the overlapping is exactly computed and the normal contact force is then proportional to the contact potential and the shear contact force is finally calculated according to the Coulomb model, as introduced previously.

To realistically model the movement of the discrete particles, viscous damping is needed to be implemented into FDEM. A damping coefficient is incorporated into the constitutive model

in FDEM, which is the so-called critical damping technique, one of the simplest approaches that have been used in many explicit FDEM. However, it was noted that the convergence rate of the critical damping technique is rather poor. Correspondingly, a local damping with a mass scaling technique is implemented into the GPGPU-parallelized HFDEM IDE code following Eq. 6:

$$\mathbf{M}^{scale} \, \partial^2 \mathbf{u} / \partial t^2 = \mathbf{f}_{tot} + \alpha \|\mathbf{f}_{tot}\| sgn(\mathbf{v}) \tag{6}$$

where M^{scale} is the scaled lumped mass, f_{tot} is the nodal out-of-balance-force, v is the nodal velocity, $\|f_{\text{tot}}\|$ is the absolute value of each component of f_{tot} , $\text{sgn}(\cdot)$ is the sign function automatically determined by the sign of (\cdot) and α is the local damping coefficient.

3 HYBRID FINITE-DISCRETE ELEMENT MODELLING OF THE COLLAPSE PROCESS OF COHESIVELESS SOIL HEAPS UNDER GRAVITY

Chen and Wang (2019) conducted a simple 2D modelling of the collapse process of a rectangular non-cohesive soil heap under gravity using a sequential 2D finite-discrete element method, in which 7142 constant-strain triangular elements are used to represent the rectangular soil heap with a size of 4 m x 2 m and the calculation takes 298.6 hours. The same model is adopted in this study but is extended into 3D to become a cuboid non-cohesive soil heaps, which has a size of 4 m x 2 m x 2m, as shown in Fig. 4 a. Characteristic element size for the soil heap is 0.05 m. Correspondingly, the soil heaps are discretized into several ten thousands of four-node tetrahedral elements, each of which is regarded as non-cohesive.

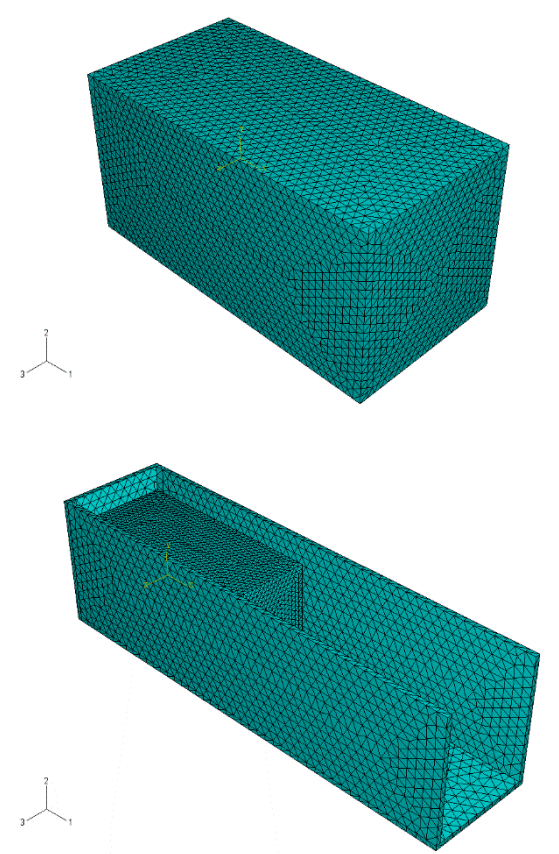


Figure 4. Numerical model of the non-cohesive soil heap and its support

In Fig. 4, the support is made of steel, whose physical-mechanical properties are listed in Table 1 together with those of the soil heap. The friction coefficient between the soil particles

and that between the soil particle and the steel surface are both defined as 0.6. The support is fixed and only gravity is applied to the soil heaps. Time step is 0.1 micro-seconds. Thanks to the GPGPU-parallelization, the running time is about 10 hours, which is much shorter than 298.6 hours required by the 2D modelling with less elements of Chen and Wang (2019).

Table 1. Physical-mechanical properties of the soil heap and its support

Properties	Soil	Support
Young's modulus	1.8	200,000
(MPa)		
Poisson's ratio	0.3	0.3
Density (kg/m ³)	1850	7800
Friction angle (°)	25	N/A

Fig. 5 depicts the modelled failure process of the soil heaps at representative time from the GPGPU-parallelized HFDEM modelling. The representative time is deliberately chosen as the same as that in the 2D FDEM modelling of Chen and Wang (2019) and the 2D SPH modelling of Bui et al. (2008). It is understandable that the non-cohesive soil collapses naturally under self-weight due to gravity since there is no support in the right side.

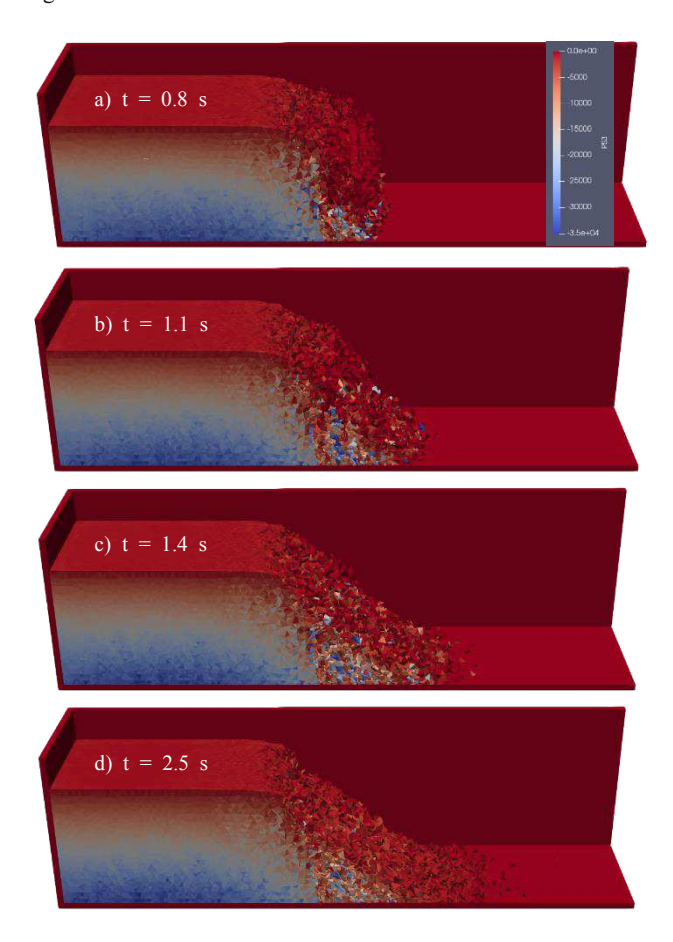


Figure 5. 3D modelling of the failure process of non-cohesive soil heaps

It can be seen from Fig. 5 that the large deformation and failure of soil heaps have been well simulated. Moreover, it is found that the parameter of local damping has an important influence on the repose angle and the horizontal running distance. In Fig. 5, the local damping coefficient is chosen as 0.08 so that the maximum horizontal running distance of the soil particle becomes consistent with that from the 2D modelling of Bui et al. (2008). With the local damping coefficient of 0.08, the

modelled failure process of the soil heaps agree well with that from the 2D modelling of Chen and Wang (2019) and Bui et al. (2008). Once the self-weight is applied, the soil on the right side collapse, as shown in Fig. 5 a at 0.8 s, since no cohesion is considered in the GPGPU-parallelized FDEM modelling. Then, a steeper slope is formed with smaller horizontal running distance (Fig. 5b at 1.1 s). After that, the soil moves rightwards gradually (Fig. 5c at 1.4s) and eventually rests (Fig. 5d at 2.5s). As mentioned, the local damping coefficient has an important influence. A series of 3D FDEM modellings are conducted to investigate the influence, in which all other parameters are kept as the same while the local damping coefficient varies. Fig. 6 illustrates the effect of various local damping coefficients on the failure process of the soil heaps. It can be seen that both the repose angle and the horizontal running distance are affected by the local damping coefficients. A similar FDEM approach was adopted by Chen and Wang (2019) although 2D. It is interesting to note this effect is not mentioned at all.

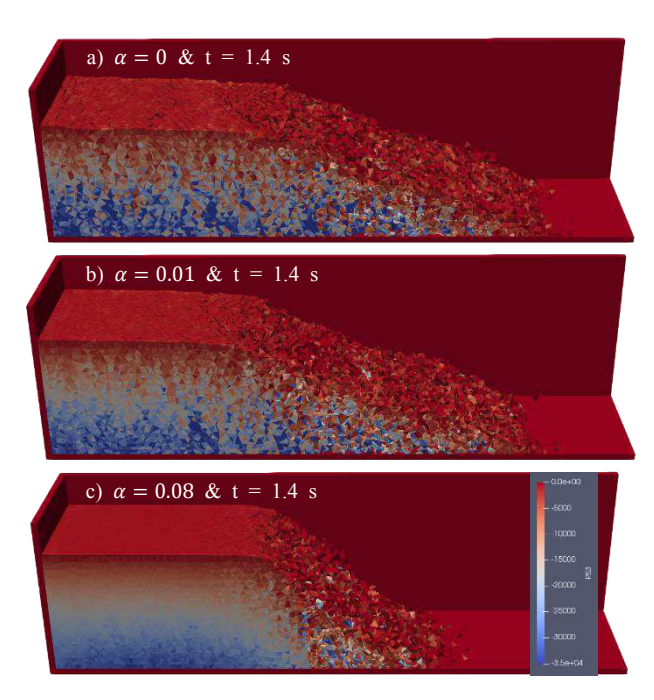


Figure 6. Effect of the local damping coefficient on the failure process of the non-cohesive soil heaps.

Besides, it should be noted that, although the maximum horizontal running distances from this 3D modelling is the same as that from the 2D modelling of Chen and Wang (2019) and Bui et al. (2008), the repose angle from the 3D modelling is much steeper, which are probably caused by the irregular shape of the soil particles. In the 2D SPH modelling by Bui et al. (2008), circular particles were adopted while triangular particles were in the 2D FDEM modelling by Chen and Wang (2019). The repose angle from Chen and Wang (2019) is 20 degrees, which is 3 degrees higher than 17 degrees from Bui et al. (2008). The 3D four-node tetrahedral particles adopted in this study are even more irregular compared with the 2D triangular particles. Thus, it should be reasonable that a high angle of repose is obtained from the 3D FDEM modelling. To clarify the effect of the particle shape on the repose angle, the soil heaps with tetrahedral parameters in Fig. 4 are replaced by using irregular-shaped Voronoi particles, as shown in Fig. 7. These irregular-shaped Voronoi particles are first generated using Neper (Query et al., 2011) and then meshed using Gmsh (Geuzaine and Remacle, 2009). They are then imported into the GPGPU-parallelized HFDEM to replace the soil heaps in Fig. 4 while the supports are

kept as the same. To save the pages, the corresponding results are not presented here but will be presented elsewhere.

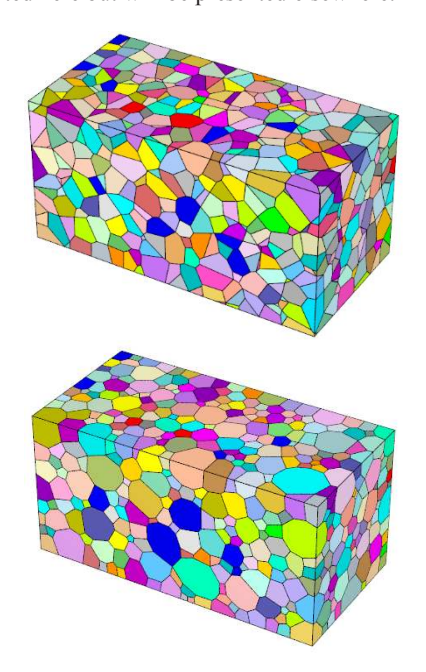


Figure 7. Non-cohesive soil heaps consisting of irregular-shaped Voronoi particles.

4 EXCAVATION-INDUCED SLOPE INSTABILITY AND DEBRIS FRAGMENTATION AND FLOW

In this section, numerical simulations are conducted using the GPGPU-parallelized HFDEM to demonstrate its ability in modelling excavation-induced instability and resultant debris fragmentation and flow. The numerical model is depicted in Fig. 8, which has a size of 100 m x 200 m. Geostatic stress analysis is firstly conducted to obtain the initial stress fields due to the self-weight of the ground using the GPGPU-parallelized HFDEM with the local damping scheme. Once static equilibrium is achieved, the ground in the right side is excavated. At the same time, both non-cohesive and cohesive elements are inserted between triangular elements in the zone bounded by the two yellow lines and other zones, respectively. After that, the excavation-induced unloading process is modelled using the GPGPU-parallelized HFDEM through the dynamic relaxation scheme with the critical damping.

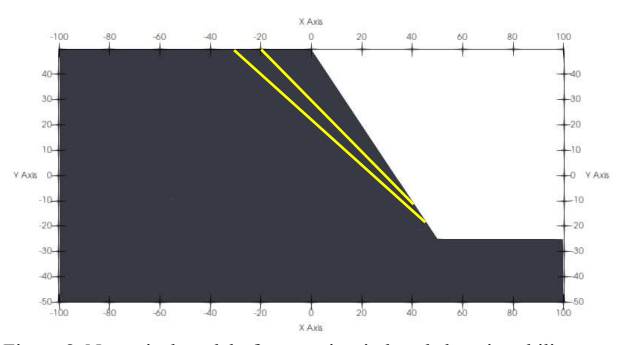


Figure 8. Numerical model of excavation-induced slope instability

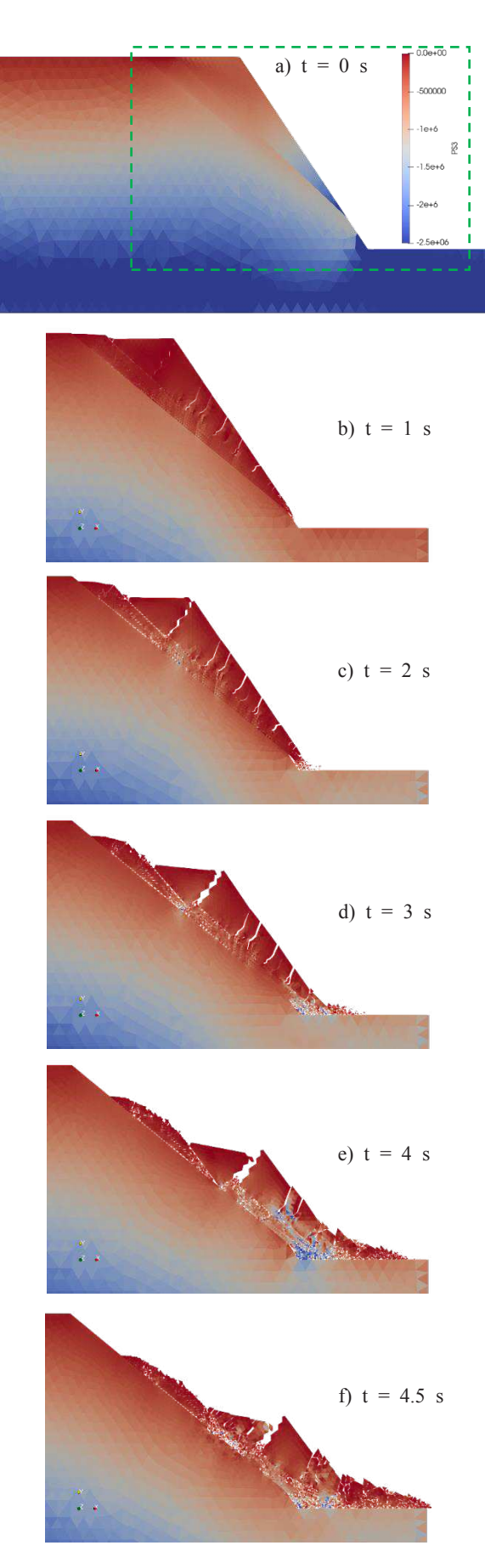


Figure 9. Excavation-induced slope instability and debris flow

Fig. 9 illustrates the excavation-induced slope instability and debris fragmentation and flow process modelled using the GPGPU-parallelized FDEM. Once the ground in the top-right part of the model is excavated, the ground on the slope loses the confinements and the movements of the slope are triggered, as shown in Fig. 9a. After that, only the area marked by the green doted lines is depicted for better visualization. As can be seen from Fig. 9b, the movement first occurs in the layer of cohesiveless ground while the grounds above the cohesive-less layer move together due to the self-weight and the loss of confinement. The inhomogeneous movements of the cohesive-less grounds result in the stress concentration happening in the initially intact ground layer above the cohesive-less ground layer. The stress concentration causes cracks are initiated and propagate to break the initially intact ground layer into various fragments moving downward the slope. At 2 s as shown in Fig. 9c, the front of the downward moving ground contacts and collides with the bench of the slope resulting in further fragmentations. After that, parts of the formed fragments and parts of the downward moving grounds fill in the toe of the slope (Fig. 9d) to form a flatter surface reducing the collisions between the downward moving ground and the bench of the slope and facilitate the debris flow (Fig. 9e). During the debris flow process, the debris further fragments to result in numerous debris, which collide with each other in complex manners and flow along the bench of the slope.

5 CONCLUSIONS

Although FDEM is nowadays widely used to investigate the fracture and failure of cohesive materials such as rocks in rock mechanics, FDEM is seldom implemented to model the physicalmechanical behaviors of non-cohesive materials such as soils in soil mechanics, which is probably due to the intensive computational costs required for the calculation of contact detection and contact interaction of irregular-shaped noncohesive particles. This study first summarizes a series of authors' recent developments greatly speeding up the contact detection and interaction calculation in FDEM, which includes GPGPU-parallelization, efficient contact activation approach, mass scaling, hyperplane separation theorem, as well as adaptive and semi-adaptive contact activation scheme. With them implemented, our GPGPU-parallelized HFDEM is about 8,000 to 61,000 times faster than the sequential FDEM code, which paves the way for investigating the instability and collapse of geo-structures and resultant debris fragmentation and flow involving in a large number of irregular-shaped non-cohesive debris. The GPGPU-parallelized HFDEM is then implemented to investigate the collapse process of 3D irregular-shaped and non-cohesive soils heaps under gravity, which is compared with others' 2D FDEM and SPH modelling. Good agreements are found among the modelled collapse process and maximum horizontal running distance if appropriate local damping coefficients are chosen. However, our modelled repose angle is much steeper than that from 2D modellings in literatures, which is probably caused by the effects of 3D irregular-shaped soil particles considered in this study. After that, the GPGPUparallelized HFDEM is applied to study the excavation-induced slope instability as well as the resultant complex debris fragmentation and flow process. It is finally concluded that the GPGPU-parallelized HFDEM provides a powerful numerical tool for investigating the instability and collapse of geostructures and resultant debris fragmentation and flow process involving in a large number of irregular-shaped non-cohesive debris.

6 REFERENCES

- An H.M., Liu H.Y., Han H., Zheng X., Wang X.G. 2017. Hybrid finitediscrete element modelling of dynamic fracture and resultant fragment casting and muck-piling by rock blast. *Computers and Geotechnics* 81:322-345
- Bui H., Fukagawa R., Sako K., Ohno S. 2008. Lagrangian meshfree particles method (SPH) for large deformation and failure lows of geomaterial using elastic-plastic soil constitutive model. *International Journal for Numerical and Analytical Methods in Geomechanics* 32: 1537-1570
- Chen X., Wang H. 2019. Slope failure of noncohesive media modelled with the combined finite-discrete element method. *Applied Science* 9: 579; doi: 10.3390/app9030579
- Fukuda D., Liu H.Y., Zhang Q., Zhao J., Kodama J., Fujii Y., Chan A. 2021. Modelling of rock dynamic fracture process using the finitediscrete element method with a novel and efficient contact activation scheme. *Int J Rock Mech Min Sci* 138: 104645.
- Fukuda D., Mohammadnejad M., Liu H.Y., Dehkhoda S., Chan A., Cho S.H., Min G.J., Han H., Kodama J., Fuji Y. 2019. Development of a GPGPU-parallelized hybrid finite discrete element method for modelling rock fracture. *International Journal for Numerical and Analytical Methods in Geomechanics* 43: 1797-1824
- Fukuda D., Mohammadnejad M., Liu H.Y., Zhang Q., Zhao J., Dehkhoda S., Chan A., Kodama J., Fuji Y. 2020. Development of a 3D hybrid finite-discrete element simulator based on GPGPU-parallelized computation for modelling rock fracturing under quasi-static and dynamic loading conditions. Rock Mech Rock Eng 53: 1079-1112.
- Geuzaine C., Remacle J.F. 2009. Gmsh: a three-dimensional finite element mesh generator with built-in pre- and post-processing facilities. *Int J Num Meth Eng* 79: 1309-1331.
- Latham J.P., Xiang J., Belayneh M., Nick H.M., Tsang C.F., Blunt M.J. 2013. Modelling stress-dependent permeability in fractured rock including effects of propagating and bending fractures. *Int J Rock Mech Min Sci* 57: 100-112.
- Lisjak A., Mahabadi O.K., He L., Tatone B.S.A., Kaifosh P., Haque S.A., Grasselli G. 2018. Acceleration of a 2D/3D finite-discrete element code for geomechanical simulations using General Purpose GPU computing. *Computers and Geotechnics* 100:84-96.
- Liu H.Y., Han H., An H.M., Shi J.J. 2016. Hybrid finite-discrete element modelling of asperity degradation and gouge grinding during direct shearing of rough rock joints. *International Journal of Coal Science* & Technology 3:295-310
- Liu H.Y., Kang Y.M., Lin P. 2015. Hybrid finite-discrete element modeling of geomaterials fracture and fragment muck-piling. *International Journal of Geotechnical Engineering* 9: 115-131.
- Mohammadnejad M., Fukuda D., Liu H.Y., Dehkhoda S., Chan A. 2020. GPGPU-parallelized 3D combined finite-discrete element modelling of rock fracture with adaptive contact activation approach. Computational Particle Mechanics 7: 849-867.
- Munjiza A. 2004. The Combined Finite-Discrete Element Method. Wiley.
- Munjiza A., Owen D.R.J., Bicanic N. 1995. A combined finite-discrete element method in transient dynamics of fracturing solids. *Engineering Computations* 12: 145-174.
- Query R., Dowson P.R., Barbe F. 2011. Large-scale 3D random polycrystals for the finite element method: generation, meshing and remeshing. Comp Meth Appl Mech Eng 200: 1729-1745.
- Rougier E., Knight E.E., Broome S.T., Sussman A.J., Munjiza A. 2014. Validation of a three-dimensional Finite-Discrete Element Method using experimental results of the Split Hopkinson Pressure Bar test. International Journal of Rock Mechanics and Mining Sciences 70: 101-108